Exact and efficient cone-beam reconstruction algorithm for a short-scan circle combined with various lines

Frank Dennerlein[a,b], Alexander Katsevich[c], Guenter Lauritsch[a] and Joachim Hornegger[b]

[a]Siemens Medical Solutions, Siemensstr. 1, 91301 Forchheim, Germany
[b]University of Erlangen-Nuremberg, Dept. of Computer Science, 91058 Erlangen, Germany
[c]University of Central Florida, Mathematics Department, Orlando, FL 32816-1364, USA

ABSTRACT

X-ray 3D rotational angiography based on C-arm systems has become a versatile and established tomographic imaging modality for high contrast objects in interventional environment. Improvements in data acquisition, e.g. by use of flat panel detectors, will enable C-arm systems to resolve even low-contrast details. However, further progress will be limited by the incompleteness of data acquisition on the conventional short-scan circular source trajectories. Cone artifacts, which result from that incompleteness, significantly degrade image quality by severe smearing and shading. To assure data completeness a combination of a partial circle with one or several line segments is investigated. A new and efficient reconstruction algorithm is deduced from a general inversion formula based on 3D Radon theory. The method is theoretically exact, possesses shift-invariant filtered backprojection (FBP) structure, and solves the long object problem. The algorithm is flexible in dealing with various circle and line configurations. The reconstruction method requires nothing more than the theoretically minimum length of scan trajectory. It consists of a conventional short-scan circle and a line segment approximately twice as long as the height of the region-of-interest. Geometrical deviations from the ideal source trajectory are considered in the implementation in order to handle data of real C-arm systems. Reconstruction results show excellent image quality free of cone artifacts. The proposed scan trajectory and reconstruction algorithm assure excellent image quality and allow low-contrast tomographic imaging with C-arm based cone-beam systems. The method can be implemented without any hardware modifications on systems commercially available today.

Keywords: image reconstruction, computed tomography, cone-beam, theoretically exact, filtered backprojection algorithm, C-arm imaging, circle and line, data completeness, geometric calibration

1. INTRODUCTION

Tomographic imaging of high contrast objects based on cone-beam projections acquired on C-arm systems[1] has already been established in a clinical, interventional environment. In particular in neuroradiology the 3D representation of the complex vascular tree is of high clinical value to plan or validate therapy. Due to the invasive, arterial injection of contrast agent the vascular tree possesses a much higher contrast to the surrounding tissue like e.g. bone. Thus, the procedure is relatively insensitive to distortions and image artifacts. Recent improvements in data acquisition, e.g. by use of flat panel detectors, will shift clinical applications towards imaging of low-contrast objects. E.g. diagnosis and treatment of stroke on the same C-arm device might be a highly desirable goal. For that hemorrhage in brain matter has to be ruled out before treating ischemia. According to current clinical protocols this is done by a native computed tomography (CT) scan. Certainly soft tissue imaging requires accurate data acquisition and processing[2].[3] A serious limitation is the incompleteness of projection data acquired by a conventional short-scan circular source trajectory. Cone artifacts, which result from that incompleteness, occur as a smearing and shading artifact and may superpose severely important low contrast details.

Numerous investigations on source trajectories which satisfy Tuy's completeness condition[4] can be found in the literature: saddle trajectory,[5] a selection of non-planar, non-closed trajectories optimized for C-arm devices,[6] circle and arc trajectory optimized for CT gantries,[7] circle and line trajectory[8][9],[10] and many others. This paper deals with a short-scan circle and line trajectory which can be easily realized on existing C-arm device without any hardware modifications. The line scan can be regarded as an add-on to the conventional short-scan circular path. To our knowledge there does not exist an exact inversion scheme for that trajectory besides the recently published algorithm of Katsevich.[11] The method is deduced from a general inversion formula based on 3D Radon theory.[15] The approach is theoretically exact, possesses efficient, shift-invariant filtered backprojection (FBP) structure, and solves the long object problem. The algorithm is flexible in dealing with various circle and line configurations. The reconstruction method requires nothing more than the theoretically minimum length of scan trajectory.

The proposed reconstruction algorithm is based on an ideal source trajectory. However, C-arm devices show some mechanical instabilities which have to be considered.[13] Fortunately, the geometrical deviations from the ideal source path are almost reproducible and are accounted for by a geometrical calibration process. The projection geometry of non-ideal source trajectories is described conveniently in the framework of projection matrices.[14] The backprojection step is performed exactly by a direct use of projection matrices. The filtering step requires a more elaborate adaptation strategy. This paper proposes a simple but robust scheme how to adapt the reconstruction algorithm to non-ideal sampling patterns as they occur in imaging with real world C-arm devices.

This paper is organized as follows: Section 2 describes the inversion formula for ideal short-scan circle and lines trajectories. The adaptation of the algorithm to source paths deviating form the ideal trajectory is presented in Section 3. Image results are shown in Section 4 which prove the clinical relevance of the requirement of complete data acquisition and validate the proposed reconstruction algorithm and its adaptation to realistic sampling patterns.

2. INVERSION FORMULA

Consider the source trajectory consisting of an incomplete circle C and a line segment L attached to C at one of the endpoints of C (see Figure 1). At first we assume that C is sufficiently close to a complete circle, and L is sufficiently long. Let y_0 be the point where they intersect. We assume that the detector array $DP(s)$ is flat, contains the x_3-axis (the axis of C), and is perpendicular to the shortest line segment connecting the source $y(s)$ and the x_3-axis.

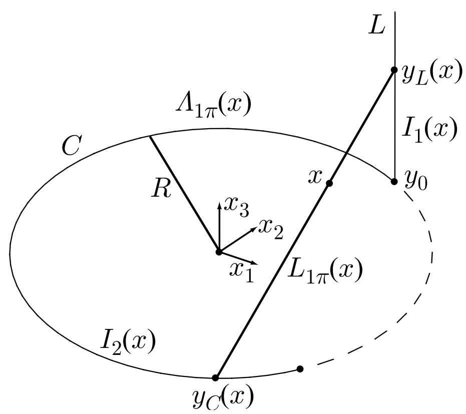

Figure 1. Illustration of the circle and line trajectory

Introduce the following notations. S^2 is the unit sphere in $\mathbb{R}^3$, and

$$\begin{aligned} D_f(y,\Theta) &:= \int_0^\infty f(y+\Theta t)dt,\ \ \Theta \in S^2; \\ \beta(s,x) &:= \frac{x-y(s)}{|x-y(s)|}; \\ \Pi(x,\xi) &:= \{z \in \mathbb{R}^3 :\ (z-x)\cdot\xi = 0\}. \end{aligned} \tag{1}$$

We assume that f is smooth, compactly supported, and identically equals zero in a neighborhood of the source trajectory.

Suppose $I_1 \ni s \to y(s) \in L$ and $I_2 \ni s \to y(s) \in C$ are parametrizations of the line and circle, respectively. We assume that the circle is of radius R and centered at the origin. Let U be an open set, such that $U \subset \{(x_1, x_2, x_3) \in \mathbb{R}^3 : x_1^2 + x_2^2 < R^2\}$.

Pick a reconstruction point $x \in U$, and consider the plane $\Pi(x)$ through x and L. $\Pi(x)$ intersects C at two points. One of them is y_0, and the second is denoted $y_C(x)$. Let $L_{1\pi}(x)$ be the line segment containing x and connecting $y_C(x)$ to L (see Figure 1). Then $y_L(x) \in L$ denotes the other endpoint of $L_{1\pi}(x)$. Our procedure determines two parametric intervals. The first one $I_1(x) \subset I_1$ corresponds to the section of L between y_0 and $y_L(x)$. The second one $I_2(x) \subset I_2$ corresponds to the section of C between y_0 and $y_C(x)$. The section of $C \cup L$ bounded by $L_{1\pi}(x)$ is denoted $\Lambda_{1\pi}(x)$. It is easily seen that $\Lambda_{1\pi}(x)$ is complete in the sense of Tuy.

Consider intersections of planes through x with $\Lambda_{1\pi}(x)$. Neglecting planes tangent to the trajectory, there can be either one or three intersection points (IPs). Moreover, there can be at most one IP belonging to L. In view of this argument, the data in Table 1 defines the weight function n up to a set of measure zero.

The role of n is twofold. First, it has to deal with redundancy in the cone beam data by assigning weights to IPs between Radon planes and the source trajectory. Second, a proper choice of n yields an efficient shift-invariant convolution backprojection algorithm in the framework of Katsevich's general inversion formula.[15] The function n, described by Table 1, can be described as follows. If there is one IP, it is given weight 1. If there are three IPs, the two IPs on the circle have weight 1 each, and the IP on the line segment has weight -1. As is easily seen, n is normalized: $\sum_j n(s_j, x, \alpha) = 1$ for almost all $\alpha \in S^2$. Here the summation is over all intersection points $y(s_j) \in \Pi(x, \alpha) \cap \Lambda_{1\pi}(x)$.

Table 1. Definition of the weight function $n(s, x, \alpha)$

Case	n
1IP, $s_1 \in I_1(x)$	$n(s_1, x, \alpha) = 1$
1IP, $s_1 \in I_2(x)$	$n(s_1, x, \alpha) = 1$
3IPs, $s_1 \in I_1(x)$ $s_2, s_3 \in I_2(x)$	$n(s_1, x, \alpha) = -1$ $n(s_k, x, \alpha) = 1, k = 2, 3$

Denote

$$\phi(s, x, \theta) := sgn(\alpha \cdot \dot{y}(s)) n(s, x, \alpha),\ \ \alpha = \alpha(\theta) \in \beta^{\perp}(s, x), \tag{2}$$

where θ is a polar angle in the plane perpendicular to $\beta(s, x)$. According to the general scheme in,[15] we have to locate jumps of $\phi(s, x, \theta)$ in θ. By studying these jumps in two cases: $s \in I_1(x)$ and $s \in I_2(x)$ and using the general scheme in[15] we obtain the following inversion algorithm (see[11]). Pick $s \in I_1(x)$ (i.e., $y(s)$ is on the line). Find a plane through x and $y(s)$, which is tangent to C at some $y_t(s, x), s \in I_2(x)$. Let $u_1(s, x)$ be the unit vector perpendicular to that plane:

$$u_1(s, x) := \frac{(y_t(s, x) - y(s)) \times \beta(s, x)}{|(y_t(s, x) - y(s)) \times \beta(s, x)|},\ \ x \in U, s \in I_1(x). \tag{3}$$

Pick now $s \in I_2(x)$ (i.e., $y(s)$ is on the circle) and define

$$u_2(s, x) := \frac{\dot{y}(s) \times \beta(s, x)}{|\dot{y}(s) \times \beta(s, x)|},\ \ x \in U, s \in I_2(x). \tag{4}$$

By construction, $u_2(s, x)$ is the unit vector perpendicular to the plane containing x, $y(s)$, and tangent to C at $y(s)$. Using (3) and (4) we obtain the following reconstruction formula for $f \in C_0^{\infty}(U)$:

$$f(x) = -\frac{1}{2\pi^2} \sum_{k=1}^{2} \int_{I_k(x)} \frac{\delta_k(s, x)}{|x - y(s)|} \int_0^{2\pi} \frac{\partial}{\partial q} D_f\left(y(q),\, \Theta_k(s, x, \gamma)\right)\Big|_{q=s} \frac{d\gamma}{\sin\gamma} ds, \tag{5}$$

where

$$\Theta_k(s, x, \gamma) := \cos\gamma \beta(s, x) + \sin\gamma e_k(s, x),\ \ e_k(s, x) := \beta(s, x) \times u_k(s, x). \tag{6}$$

and δ_k is defined as follows:

$$\delta_1(s,x) = -sgn(u_1(s,x)\cdot\dot{y}(s)),\ s\in I_1(x);\quad \delta_2(s,x)=1,\ s\in I_2(x). \tag{7}$$

Suppose, for example, that L is parametrized in such a way that the source moves down along L as s increases. Then $\delta_1(s,x)=1, s\in I_1(x)$. If the source moves up along L as s increases, then $\delta_1(s,x)=-1, s\in I_1(x)$.

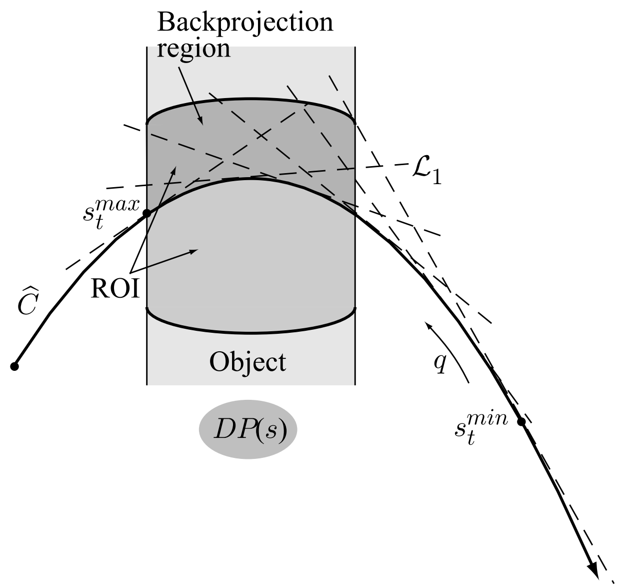

Figure 2. Projection onto the detector plane when the source is on the line

Consider now the computational structure of the algorithm. Pick $y(s)\in L$. For a point $x\in U$ we have to find $s_t\in I_2(x)$. This determines the filtering line on the detector, which is tangent to $\hat{C}$ at $\hat{y}(s_t)$. Here $\hat{C}$ and $\hat{y}(s_t)$ are projections onto the detector plane of C and $y(s_t)$, respectively. It is easy to see that all other $x\in U$ which project onto this line to the left of $y(s_t)$ will share it as their filtering line. Hence, we can first perform filtering along lines on the detector tangent to $\hat{C}$ (see family $\mathcal{L}_1$ in Figure 2), and then perform backprojection. The range of s_t values, $s_t^{min}\le s_t\le s_t^{max}$, depends on the region of interest (ROI) and is illustrated in Figure 2. Just like in[15] it is easily seen that filtering is shift-invariant, and consists of convolving $\frac{\partial}{\partial q}D_f\left(y(q),\,\Theta_k(s,\cdot,\gamma)\right)|_{q=s}$ with $1/\sin\gamma$.

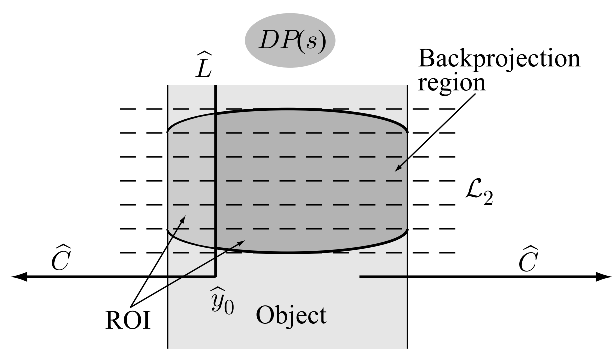

Figure 3. Projection onto the detector plane when the source is on the circle

If $y(s)\in C$, filtering must be performed along lines on the detector parallel to $\dot{y}(s)$. The resulting family is denoted $\mathcal{L}_2$ in Figure 3. Pick any line from $\mathcal{L}_2$. One shows that all x whose projection belongs to that line and appears to the right of $\hat{L}$ share it as their filtering line. As before, one can first perform filtering (i.e., convolution with $1/\sin\gamma$) along these lines, and follow it by backprojection. Hence the resulting algorithm is of the convolution-based FBP type.

Let us now describe some properties of the proposed algorithm. As follows from the construction of $L_{1\pi}(x)$, $y_L(x) \to y_0$ as $x_3 \to 0$. In the limit $x_3 = 0$ we get $y_L(x) = y_0$, so the integral over L in (5) disappears, and the integral over C becomes a very short scan fan-beam reconstruction formula of.[17]

Given specific C and L, we can determine the part of the support of f that can be accurately reconstructed by the proposed algorithm. This is the volume bounded by the following three surfaces: the plane of C, the plane defined by L and the endpoint of C not on L, and the conical surface of lines joining the points of C to the endpoint of L that is not on C. This volume will be denoted $U(C, L)$. Note however that the object f may extend outside $U(C, L)$, as long as it stays away from the source trajectory $C \cup L$.

The trajectory consisting of an incomplete circle and a line segment can be used as a building block for constructing other trajectories. E.g., one can consider an incomplete circle C with line segments attached to it at each endpoint of C. These segments can be on opposite sides of C (see Figure 4, left panel), or on the same side of C (see Figure 4, right panel). Inversion algorithms for these trajectories are obtained from (5) by applying it to each circle+line subset and then adding the results (if necessary). Indeed, suppose the segments are on opposite sides of C. Then the volume $U(C, L)$ in the half-space $z \geq 0$ is reconstructed using the trajectory $C \cup L$, and the volume $U(C, L')$ in $z \leq 0$ is reconstructed using $C \cup L'$. In this case no summation is needed. If L and L' are on the same side of C, then we only reconstruct in the half-space $z \geq 0$. In this case each voxel in the volume $U(C, L) \cap U(C, L')$ is reconstructed twice: using $C \cup L$ and $C \cup L'$, so the summation is used. This does not mean that reconstruction time is twice as long. First, the line portions of the scan L and L' are used only one time each. Second, only a part of the circle C is used twice. This does not lead to any increase in computational time, because filtering and backprojection are identical in both cases. Consequently, a simple post-filtering weight solves the problem of multiple contributions to any given voxel.

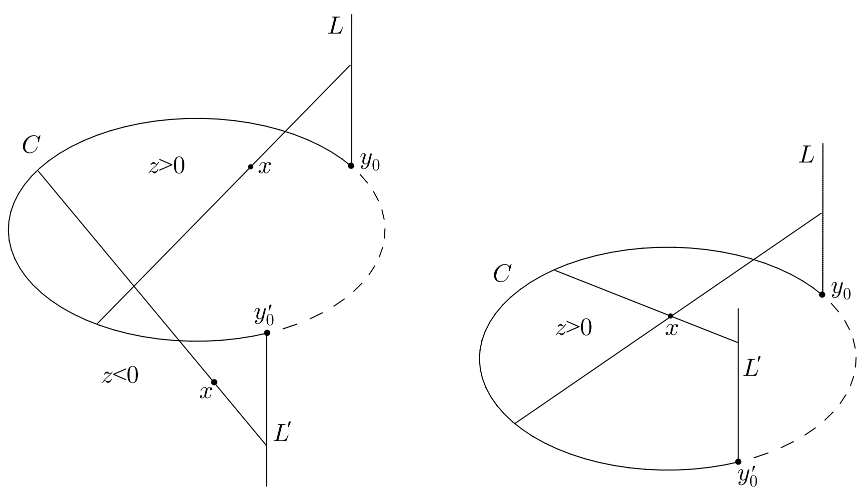

Figure 4. Examples of trajectories that can be handled by the proposed algorithm

Consider now the overall detector requirements. We will assume that L and L' are on the opposite sides of C, and the reconstruction volume is $\{(x_1, x_2, x_3) : \ x_1^2 + x_2^2 \leq r^2, \ -H \leq x_3 \leq H\}$. It is easily seen that the circular scan requires the rectangular detector of size

$$|d_1| \leq \frac{r}{\sqrt{1-(r/R)^2}}, \ |d_2| \leq \frac{H}{1-(r/R)}. \tag{8}$$

Here d_1 and d_2 are the horizontal and vertical axes on the detector. It is shown in[11] that the line scans require the detector of size

$$|d_1| \leq \frac{r}{\sqrt{1-(r/R)^2}}, \ |d_2| \leq \frac{H}{1-(r/R)}\frac{1}{1-(r/R)^2}. \tag{9}$$

Hence the addition of line scans increases the detector height compared with the conventional Feldkamp-type circular reconstruction only by a factor $1/(1-(r/R)^2)$.

3. CONSIDERATION OF NON-IDEAL SOURCE TRAJECTORIES

The exact reconstruction algorithm derived in the previous section presumes on an ideal acquisition geometry. Data acquisition with a C-arm device, however, never fulfills these ideal geometry presumptions. The movements of the acquisition system are influenced by mechanical phenomena like gravity and inertia leading to different non-ideal types of focus trajectories - a phenomena that has to be considered in the reconstruction approach.

3.1. Geometry description using Projection Matrices

The non-ideal acquisition geometry of a real world C arm device now is represented by a sequence of homogenous projection matrices[14] $P_s \in \mathbb{R}^{3\times4}$. For every source position s, and thus for every measured projection image, the matrix P_s completely describes the perspective cone beam projection of the object. More precisely, the matrix defines the relation between every voxel x_h of the object and the coordinates w_h of the corresponding detector image point

$$w_h = P_s x_h, \tag{10}$$

where a voxel with a cartesian coordinate vector x is denoted by the homogenous vector $x_h = (b \cdot x^T, b)$ with $b \in \mathbb{R} \setminus 0$ and an analog notation for a cartesian detector position $w = (u_{pix}, v_{pix})^T$ is $w_h = (c \cdot w^T, c)^T$, $c \in \mathbb{R} \setminus 0$. u_{pix} and v_{pix} are the coordinate values of an image point measured along the two perpendicular axes' vectors $e_{u,s}$ respectively $e_{v,s}$ that coincide with the row respectively the column direction of the pixel grid of the detector $DP(s)$.

As the deviations in acquisition geometry vary from C-arm device to C-arm device, but remain almost constant for successive scans on the same device, an essential task is to determine an individual, valid sequence of P_s for a given C-arm system. This geometric calibration is done by an automated procedure involving a calibration phantom of exactly defined structure and an appropriate calibration algorithm that calculates a valid matrix P_s for a given s.[18]

A matrix P_s can be decomposed in a complete set of projection parameters.[14] Especially the *extrinsic parameters* are of interest as they include position and orientation of the involved detector and focus entities. We present a way to calculate the focus positions and the direction vectors of the pixel coordinate system's axes from every P_s. By that the acquisition trajectory can be composed and when using matrices downloaded from a real world C-arm device, it is possible to determine the deviations of the acquisition geometry compared to the ideal circle and line geometry presumed by the reconstruction approach. For convenience the matrices $M_s \in \mathbb{R}^{3\times3}$ are introduced, consisting of the first three columns of the P_s. Note that all M_s are invertible.

The focus position $y(s)$ is calculated as

$$y(s) = M_s^{-1} P_s (0,0,0,1)^T. \tag{11}$$

The projection matrices define the detector only up to scale. To have knowledge about the precise structure of the C-arm acquisition system, either the specification of the focus-detector distance or the detector pixel spacing is needed. The direction of the two axis of the detector pixel coordinate system, however, is universally valid. $e_{u,s}$ is parallel to the vector $((0,0,1)\cdot M_s)^T \times ((0,1,0)\cdot M_s)^T$ and $e_{v,s}$ points in direction $((0,0,1)\cdot M_s)^T \times ((1,0,0)\cdot M_s)^T$. Further, the detector coordinates $w_{0,s}$ of the intersection of the optical axis and the detector plane are calculated as $w_{0,s} = M_s \cdot (0,0,1) M_s$. It turns out that the real path can vary up to 2% in radial direction from an ideal circle. Further, the focus positions are not located within a plane, but vary in longitudinal direction. We found out that a relative movement of focus and detector appears when the C-arm is in motion. Tilt and rotational deviations are not very prominent, but the translationary in-plane movement of the detector during the acquisition run is considerable. The reconstruction algorithm derived for an ideal circle and line trajectory has to be adapted to the non-ideal source paths of real C-arm devices.

3.2. Adaptations to the original method

For an application of the circle and line reconstruction approach the following general strategy is applied. The given projection matrix P_s exactly describes the relation between the object and its cone beam projection image for every s. By that, an exact consideration of the non-ideal acquisition geometry in the backprojection step is possible by the direct use of the projection matrices.[13] For the filtering step the case of non-ideal trajectory is transferred into the ideal case approximately. The presumed ideal trajectory consisting of a partial circle and a perpendicularly attached line segment is fitted into the set of real world focus positions. The fitted circle path again projects as a parabola onto the detector and the same approach as described above can be used to determine the filtering directions as tangents to the occurring parabola.

The least-square fit of the ideal trajectory $y_{fitted}(s)$ into the path $y(s)$, as illustrated in Figure 5 corresponds to the minimization of the total estimation error

$$\epsilon = \sum_s \left(\|y_{fitted}(s) - y(s)\|^2 \right) \tag{12}$$

and is done in a three steps approach.

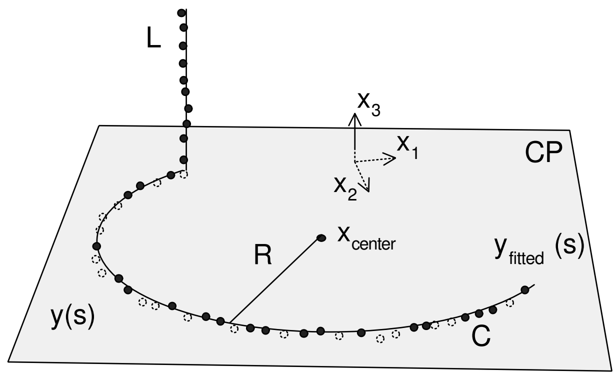

Figure 5. Fit of an ideal circle and line trajectory $y_{fitted}(s)$ into the set of real world focus positions $y(s)$. A dotted object is located below the circular plane CP.

First, we perform a least-square algebraic fit of a plane into the circle's focus positions followed by an orthogonal projection of the path $y(s)$ onto the determined circular plane CP. On CP, a partial circle is fitted into the projected focus positions using a 2D algebraic least-square estimation method[19] and then optimally represents the circle scan. Finally the line segment is determined perpendicular to the circular plane and connected to the end of the circle segment. The fitted trajectory can be described by the circular plane CP, the circle center x_{center}, the circle segment's radius R and the length and the position of the line segment.

Remember that the pose and the orientation of the volume coordinate system are given by the projection matrices P_s. We perform a normalization of the coordinate system bringing it more in line with the configuration of the previous chapter. This is done by multiplying every P_s from the right side with a transformation matrix $T_v \in \mathbb{R}^{4\times4}$ independent from s. The normalization consists of two operations, a translation $T_{v,t}$ to locate the origin at x_{center} and a rotation $T_{v,r}$ that parallelizes the line direction with the x_3 axis. We can thus write $T_v = T_{v,r} \cdot T_{v,t}$. After the coordinate transform, the circular plane CP equals the x_3=0 plane and the trajectory is centered around the rotational axis with the line pointing in positive x_3 direction.

Further, the change of the relative position of the focus and the detector has to be handled. The detector coordinate system is adapted such that the fitted source trajectory is projected onto the detector on the same position as in the ideal case. Then, the filtering instructions described in Section 2 can be applied without any further modification. Regarding the used C-arm hardware, it turns out to be sufficient to correct the in-plane translationary movement of the pixel coordinate system, which is the most prominent deviation from the ideal geometry case. For every s, a translation matrix $T_{d,s} \in \mathbb{R}^{3\times3}$ is determined and multiplied to P_s from the left, so that the volume coordinate origin always projects onto the same detector coordinates. By that, the coordinates of $\hat{C}$ become independent from the current misplacement of the detector area.

Finally, the modified projection matrices

$$P_s^{mod} = T_{d,s} \cdot P_s \cdot T_v \tag{13}$$

describe the cone beam projection involving the normalized coordinate systems for the volume and for the detector. Note that these projection matrices still represent the non-ideal acquisition geometry.

4. IMAGE RESULTS

To test the quality of the developed reconstruction method a set of experiments is performed, involving different phantom objects and ideal as well as real world non-ideal acquisition geometry.

4.1. Clinical relevance of Cone Artifacts

This evaluation proves the clinical relevance of the well known cone artifacts appearing frequently in short scan FDK reconstructed volume data sets from mathematically defined objects. We thus expect statements about the quality of the reconstruction approaches in the practical domain. In a first experiment both the state of the art short scan FDK algorithm and the circle and line approach are used to reconstruct a volume data set from synthetic projections of the so called *voxelized head phantom.* This object is defined as an array of $512 \times 512 \times 360$ voxel values $f(x)$ that represent a human head with data generated by a spiral CT Angiography imaging system.

The voxelized head phantom is centered around the plane of the circular trajectory at x_3=0. The acquisition trajectory involves 2 line segments pointing in different directions, and so the upper half of the object is reconstructed from projections acquired along the upper line and the circle, whereas the lower parts require the other line segment and the circle. Detailed reconstruction parameters are presented in Table 2.

Figure 6 and Figure 7 visualize two different slices of the reconstructed volumes as well as of the original object definition. As we want to compare image qualities in low contrast applications, a small window from -100 HU to 100 HU is selected.

Figure 6. The x_1=0 mm slice of the voxelized head phantom, visualized in a window of -100 HU to +100 HU. From the left to the right the short scan FDK result, the circle and line result and the original image are shown.

Regarding first the slice x_3=-59 mm of Figure 7, including a lot of bone structures and thus rich in contrast, one can see that the cone artifacts are very prominent in the image reconstructed by the short scan FDK approach. Smearing artifacts cover up the view on the soft tissue decreasing the significance of the image content strongly. In the less structured regions of the voxelized head phantom, like in the brain region, however, only few disturbing cone artifacts are visible. The circle and line approach overcomes the restriction of an incompletely acquired 3D Radon space and thus can eliminate the cone artifact phenomena throughout the whole volume. The image results are very close and almost not distinguishable to the original object in both visualized slices.

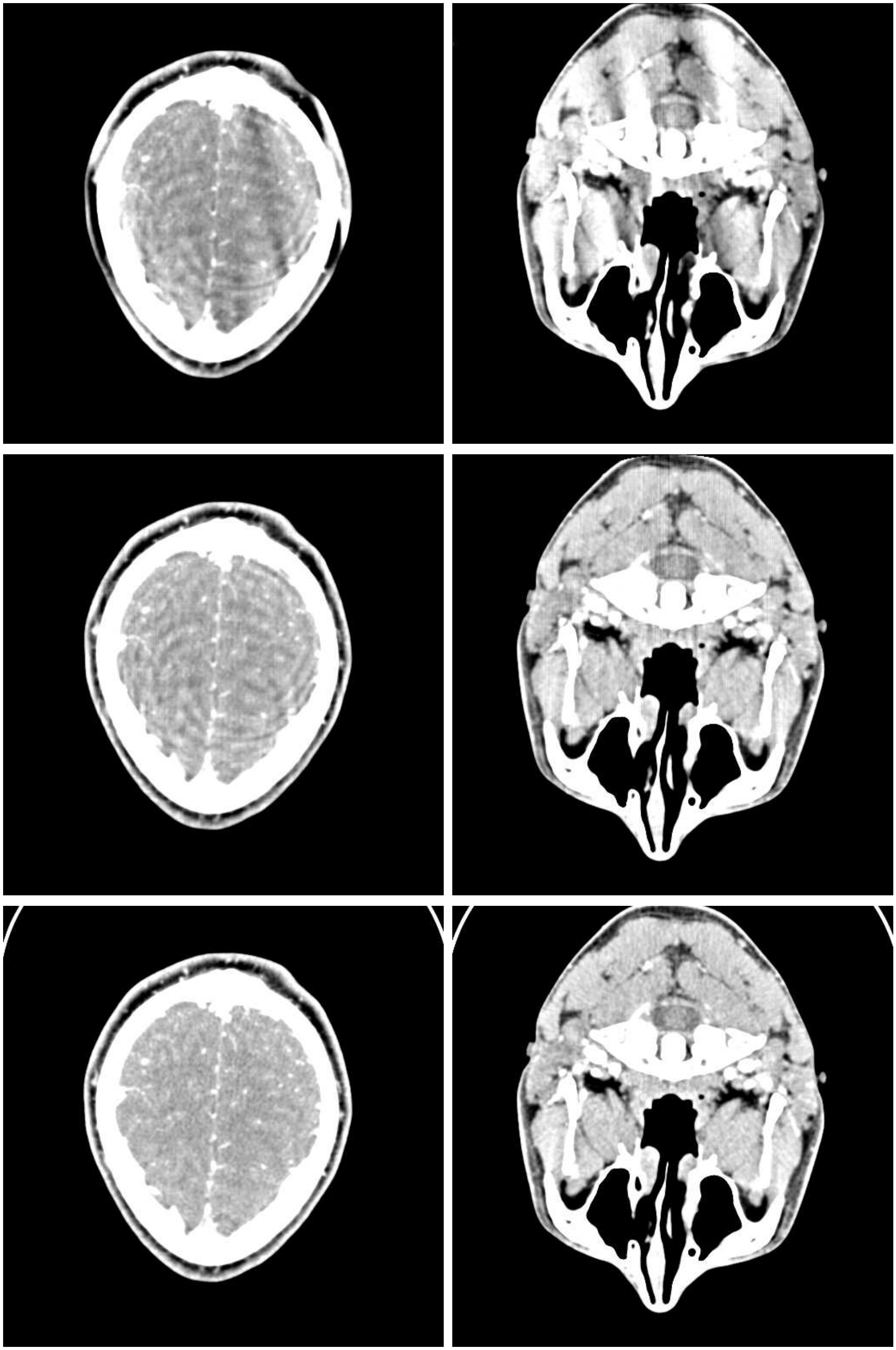

Figure 7. Transaxial slices taken from the voxelized head phantom and visualized with a window from -100 HU to +100 HU. Row-wise from the top to the bottom: Image results when using the short scan FDK method, the circle and line approach and the original slices. The left column shows the slice x_3=+59 mm the right one x_3=-59 mm.

4.2. Qualitative Analysis using non-ideal Geometry

In a second experiment we involve the non-ideal acquisition geometry corresponding to a real world C-arm scan in order to validate the proposed adaption scheme. Further, the effects of the geometry deviations on the quality of the resulting images is shown.

The object of interest is now composed by mathematically defined geometric objects like ellipsoids or cubes and simulates the basic anatomical structure of a human head including homogeneous regions with embedded low contrast objects but also high contrast structures. Because of its composition, this so called *mathematical head phantom*[20] is very demanding to the reconstruction approaches significantly revealing any type of artifact.

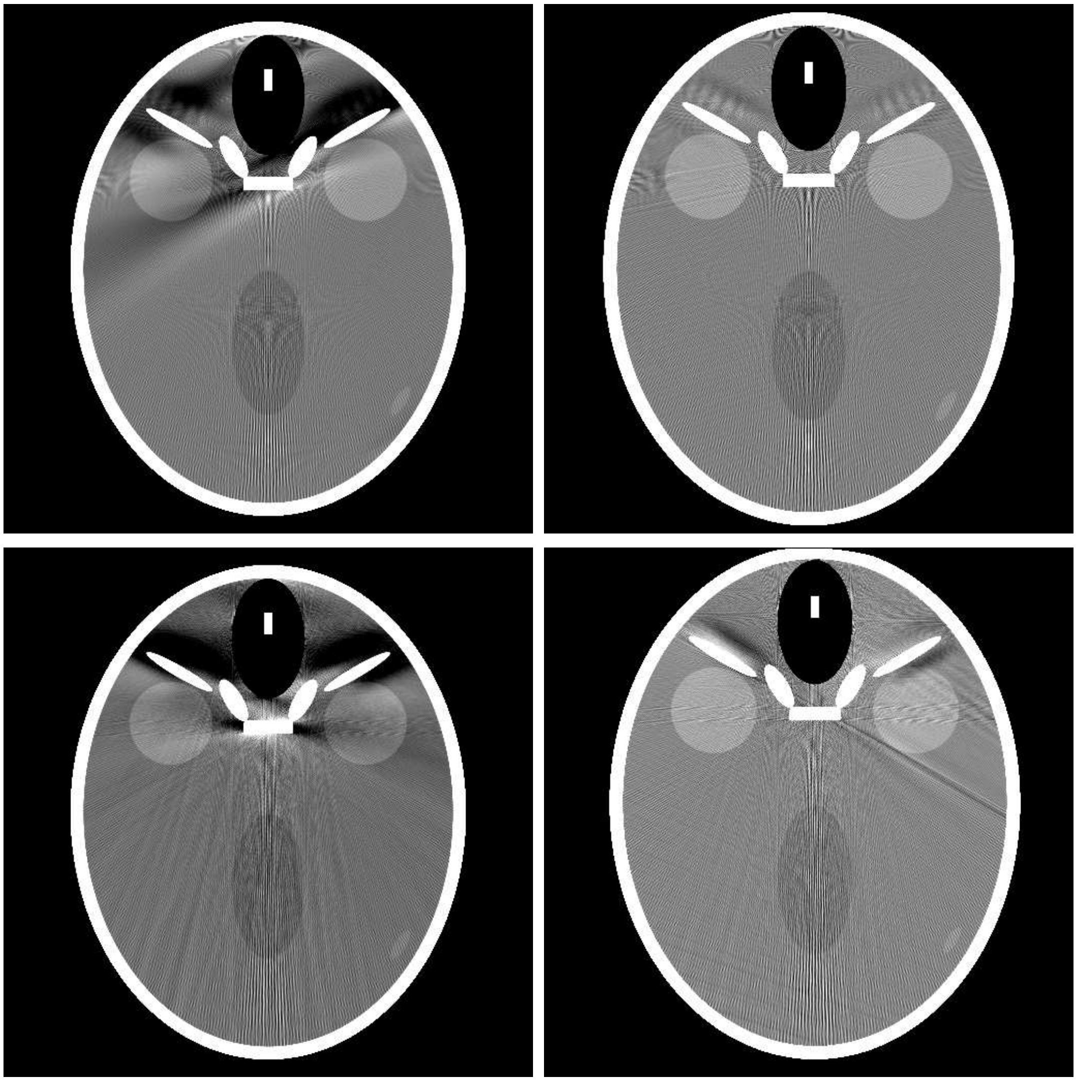

Figure 8. The slice x_3=49.5mm visualized using a window from 10 HU to 90 HU. The top row presents the results from the ideal geometry simulation, the the bottom row from the simulation involving real, non-ideal acquisition geometry. The images on the left are reconstructed using the short scan FDK method, the images on the right using the circle and line approach.

Two scans are simulated from the object, which is shifted by 4 cm along the x_3 axis. The first one involves ideal geometry and the second one includes a series of projection matrices downloaded from a real world C-arm device and thus representing relevant geometry deviations. The reconstruction and simulation parameters are listed in Table 2.

In Figure 8 one representative transaxial slice of the object is visualized in a window from 10 HU to 90 HU. The experiments affirm the results from the first evaluation. Again, severe cone artifacts appear in the FDK reconstructed images in contrast to the high quality image data resulting from the circle and line method. Note that the simulated scans of ideal and non-ideal trajectories start at different angular positions. Thus, the orientation of artifacts differ. Involving non-ideal acquisition geometry, additional artifacts in both reconstruction approaches can be detected. Some streak-like artifacts of low intensity appear near the high contrast bone structure. The artifacts are due to some slight irregularities in angular sampling and to some remaining inexactness in the filtering step. In particular the matching of the contribution of the line and circular scan might be critical in more severe cases. Anyway, this experiment shows that the proposed adaptation appears sufficient to consider geometrical distortions of real world C-arm devices.

	voxelized head	mathematical head	
	ideal geometry	ideal geometry	non-ideal geometry
detector dimension	641×500	640×500	720×720
pixel size	$(0.6\text{mm})^2$	$(0.6\text{mm})^2$	$(0.580\text{mm})^2$
# projections on circle	501	501	538
# projections on each line	221	196	196
angular range of circle	200 deg	200 deg	214 deg
length of each line	220 mm	195 mm	195 mm
image volume dimension	$512 \times 512 \times 400$	$512 \times 512 \times 161$	$512 \times 512 \times 161$
voxel size	$(0.422\text{mm})^3$	$0.48 \times 0.48 \times 0.50\text{mm}^3$	$0.48 \times 0.48 \times 0.50\text{mm}^3$

Table 2. Reconstruction and simulation parameters

5. CONCLUSIONS

C-arm based tomographic imaging is developing rapidly towards low contrast resolution. A severe obstacle is the fact that a pure circular scan path does not provide a complete dataset in cone-beam geometry. A simulation study with an anthropomorphic head phantom clearly shows the clinical relevance of cone artifacts resulting from data incompleteness. Data incompleteness can be overcome by an additional line scan to the conventional short-scan circular trajectory. The line scan can be easily realized as an add-on to current C-arm devices without any hardware modifications. A recently published reconstruction algorithm of Katsevich type handles the case of an ideal trajectory theoretically exact and efficient requiring a minimum amount of data. A stable method is proposed to adapt approximately the reconstruction algorithm to the real sampling pattern of existing C-arm devices which deviates from the ideal source path. An ideal trajectory is fitted to the real source path to find proper filtering lines. Backprojection is performed exactly by use of the geometric calibration information. In simulation experiments it is shown that (i) the new reconstruction algorithm provides excellent image quality; (ii) cone artifacts are totally eliminated by use of a complete data set; (iii) geometrical deviations from the ideal trajectory can be handled robustly by the suggested, simple adaptation approach at least for existing C-arm devices; (iv) non-ideal trajectories still cause some slight streak artifacts due to irregular sampling and remaining inexactness of the approximate geometrical adaptation. Certainly the limitations of approximation in the adaptation approach have to be investigated systematically in the future. Furthermore a quantitative assessment of image quality is still in preparation. Anyway, it appears that the proposed approach is an easy and viable way to provide excellent low contrast imaging based on C-arm devices in a clinical, interventional environment.

ACKNOWLEDGMENTS

The work of the second author was supported in part by NSF grant DMS-0104033 and by Siemens AG, Medical Solutions.

REFERENCES

1. M. Grass, R. Koppe, E. Klotz, R. Proksa, M. Kuhn, H. Aerts, J. O. de Beck, and R. Kempkers, "Three-dimensional reconstruction of high-contrast objects using c-arm image intensifier projection data," *Comp. Med. Imag. and Graphics 23* , pp. 311–321, 1999.
2. M. Zellerhoff, B. Scholz, E.-P. Rhrnschopf, and T. Brunner, "Low contrast 3d-reconstruction from c-arm data," in *Proc. SPIE 5745 (2005) 71, to be published*, 2005.
3. J. Wiegert, M. Bertram, D. Schfer, N. Conrads, N. Noordhoek, K. de Jong, T. Aach, and G. Rose, "Soft tissue contrast resolution within the head of human cadaver by means of flat detector based cone-beam ct," in *Proc. SPIE 5368*, pp. 330–337, 2004.
4. H. K. Tuy, "An inversion formula for cone-beam reconstruction," in *SIAM J. Appl. Math*, 1983.
5. J. Pack, F. Noo, and H. Kudo, "Investigation of saddle trajectories for cardiac ct imaging in cone-beam geometry," *Phys. Med. Biol. 49* , pp. 2317–2336, 2004.
6. H. Schomberg, "Complete source trajectories for c-arm systems and a method for coping with truncated cone-beam projections," in *Proc. Meeting on Fully 3-D Image Reconstruction in Radiology and Nucl. Med.*, 2001.
7. R. Ning, X. Tang, D. Conover, and R. Yu, "Flat panel detector-based cone beam computed tomography with a circle-plus-two-arcs data acquisition orbit: Preliminary phantom study," *Med. Phys. 30* , pp. 1694–1705, 2003.
8. G. L. Zeng and G. T. Gullberg, "A cone-beam tomography algorithm for orthogonal circle-and-line orbit," *Physics in Medicine and Biology 37* , pp. 563–577, 1992.
9. R. Johnson, H. Hu, S. Haworth, P. Cho, C. Dawson, and J. Linehan, "Feldkamp and circle-and-line cone-beam reconstruction for 3d micro-ct of vascular networks," *Phys. Med. Biol. 43* , pp. 929–940, 1998.
10. H. Kudo and T. Saito, "Fast and stable cone-beam filtered backprojection method for nonplanar orbits," *Phys. Med. Biol. 43* , pp. 747–760, 1998.
11. A. Katsevich, "Image reconstruction for the circle and line trajectory," *Physics in Medicine and Biology 49* , pp. 5059–5072, 2004.
12. A. Katsevich, "A general scheme for constructing inversion algorithms for cone-beam ct," *International Journal of Mathematics and Mathematical Sciences 21* , pp. 1305–1321, 2003.
13. K. Wiesent, "Enhanced 3-d-reconstruction algorithm for c-arm systems suitable for interventional procedures," in *IEEE Transactions on Medical Imaging*, 2000.
14. R. Hartley and A. Zisserman, *Multiple View Geometry in Computer Vision*, Cambridge University Press, 2000.
15. A. Katsevich, "A general scheme for constructing inversion algorithms for cone beam CT," *International Journal of Mathematics and Mathematical Sciences* **21**, pp. 1305–1321, 2003.
16. A. Katsevich, "Image reconstruction for the circle and line trajectory," *Physics in Medicine and Biology 49* , pp. 5059–5072, 2004.
17. F. Noo, M. Defrise, R. Clackdoyle, and H. Kudo, "Image reconstruction from fan-beam projections on less than a short scan," *Physics in Medicine and Biology* **47**, pp. 2525–2546, 2002.
18. A. Rougee, C. Picard, C. Ponchut, and Y. Trousset, "Geometrical calibration of x-ray imaging chains for three-dimensional reconstruction," *Computerized Medical Imaging and Graphics 17* , pp. 295–300, 1993.
19. W. Gander, G. H. Golub, and R. Strebel, "Least-squares fitting of circles and ellipses," in *Numerical analysis (in honour of Jean Meinguet)*, editorial board Bulletin Belgian Mathematical Society, ed., pp. 63–84, 1996.
20. "http://www.imp.uni-erlangen.de/phantoms/head/head.html, head phantom description, last visited: 29.12.2004."